Blind Deconvolution Method Of Image Deblurring Using
Convergence Of Variance

THESIS

Capt Quentin D. MacManus,

AFIT/GE/ENG/11-26

DEPARTMENT OF THE AIR FORCE
AIR UNIVERSITY

AIR FORCE INSTITUTE OF TECHNOLOGY

Wright-Patterson Air Force Base, Ohio

AFIT/GE/ENG/11-26

Blind Deconvolution Method Of Image Deblurring Using Convergence Of Variance

THESIS

Presented to the Faculty

Department of Electrical and Computer Engineering

Graduate School of Engineering and Management

Air Force Institute of Technology

Air University

Air Education and Training Command

In Partial Fulfillment of the Requirements for the

Degree of Master of Science

Capt Quentin D. MacManus, B.S.E.E.

March 2011

AFIT/GE/ENG/11-26

Blind Deconvolution Method Of Image Deblurring Using Convergence Of Variance

Capt Quentin D. MacManus, B.S.E.E.

Approved:

/Signed/		10 March 2011
Dr. Richard Martin (Chairman)		Date
/Signed/		10 March 2011
Dr. Stephen Cain (Member)		Date
/Signed/		10 March 2011
Dr. Julie Jackson (Member)		Date

AFIT/GE/ENG/11-26

Abstract

Images are used for both aerial and space imagery applications, including target detection and tracking. The current problem concerning objects in geosynchronous orbit is that they are dim and hard to resolve because of their distance. This work will further the combined effort of AFIT and AFRL to provide enhanced space situational awareness (SSA) and space surveillance. SSA is critical in a time when many countries possess the technology to put satellites into orbit. Enhanced imaging technology improves the Air Force's ability to see if foreign satellites or other space hardware are operating in the vicinity of our own assets at geosynchronous orbit. Image deblurring or denoising is a crucial part of restoring images that have been distorted either by movement during the capture process, using out-of-focus optics, or atmospheric turbulence. The goal of this work is to develop a new blind deconvolution method for imaging objects at geosynchronous orbit. It will feature an expectation maximization (EM) approach to iteratively deblur an image while using the convergence of the image's variance as the stopping criteria

Acknowledgements

I would like to thank my thesis advisor, Dr. Richard Martin and committee member, Dr. Stephen Cain. Their guidance and technical support throughout this research effort was instrumental in my ability to complete it. Their expertise and advice was invaluable and greatly appreciated.

I would also like to thank my wife for her love and patience. Her support kept me going throughout this whole process.

<div align="center">Capt Quentin D. MacManus</div>

Table of Contents

List of Figures

Blind Deconvolution Method Of Image Deblurring Using Convergence Of Variance

I. Introduction

This chapter describes the problem to be addressed by this research. Background on the problem and research goals are also provided.

1.1 Motivation

Space Situational Awareness (SSA) is a key mission of the United States Air Force Space Command. One aspect of SSA involves using both telescope networks and radars to detect, identify, record and track all man-made objects orbiting the earth. Knowing the exact locations of these orbiting objects in space is crucial for future space operation safety. The SSA mission has become even more important with recent events such as Iridium and Cosmos satellite collision and the Chinese anti-satellite missile test in 2007, both of which created large swaths of space debris. This debris, known as space junk, will be an ongoing risk to US satellites for years to come as the orbits of the debris degrade toward Earth.

1.2 Background

Images are used for both aerial and space imagery applications, including target detection and tracking. The current problem concerning objects in geosynchronous orbit is that they are dim and hard to resolve because of their distance. This work will further the combined effort of AFIT and AFRL to provide enhanced SSA and space surveillance. SSA is critical in a time when many countries possess the technology to put satellites into orbit and enhanced imaging technology will improve the Air Force's ability to see if foreign satellites or other space hardware are operating in the vicinity of our own assets at geosynchronous orbit.

Image deblurring or denoising is a crucial part of restoring images that have been distorted either by movement during the capture process, using out-of-focus optics, or atmospheric turbulence. There currently exist a number of methods for image deblurring. These either use the short optical transfer function (OTF), which negates atmospheric tilt caused by phase delay, or rely on a posteriori data in order to make an estimate about the seeing parameter, which describes the effect of atmospheric turbulence. The goal of this work is to develop a new blind deconvolution method for long exposure imaging of objects at geosynchronous orbit without the need for any a posteriori data.

The proposed research effort would attempt to produce a blind deconvolution algorithm that produces useful results when processing astronomical scenes. This new technique will capitalize on the statistics of the blurry image and the refined image estimate, in an iterative approach to converge on the correct seeing parameter. This approach has the potential to perform blind deconvolution on myriad data sources and applications.

1.3 Research Goals

The expected result of this work is the development of a new approach for blind deconvolution that improves on current methods for deblurring astronomical data. Experiments conducted using simulated data will feature binary star images as well as images of satellites blurred by atmospheric turbulence. The signal to noise ratio of the data will also be varied via changes in the coherence parameter of the simulated laser illumination. Experiments using measured data will use the value of the estimated seeing parameter as a metric for success as ground truth measurements of that parameter are available for each set of measured imagery.

1.4 Thesis Organization

Chapter II provides a description of the Maximum A Posteriori (MAP) estimation algorithm and related work, attempting to solve the blind deconvolution

problem using the long exposure atmospheric transfer function. Chapter III details the methodology used in this research, and the simulations and experiments which were conducted. Chapter IV yields the results from the simulations and experiments described in Chapter III. Finally, Chapter V provides a summary for this research and suggests potential areas for follow-on research.

II. Background

This chapter provides the technical background necessary for understanding the overall concepts of this research. First, a description of blind deconvolution is provided. Next, related work is presented including an examination of both the MAP estimation and APEX techniques. The APEX method, which is not an acronym, was developed by Alfred Carasso [5]. The MAP algorithm is provided along with its derivation. Examples are provided to demonstrate how these algorithms perform on fully illuminated datasets. Finally, examples are given to show how these algorithms are not useful when processing atmospheric data, and an alternative method is suggested.

2.1 Blind Deconvolution

Deconvolution is the process of filtering a signal to compensate for an undesired convolution. This convolution operation on the data is caused by the effect of atmospheric turbulence. The goal of deconvolution is to recreate the signal as it existed before the convolution took place. This usually requires that the characteristics of the convolution are known. In this case it is assumed that the point spread function (PSF) responsible for the blurring is known.

Blind deconvolution, on the other hand, is a deconvolution technique that permits the recovery of the target scene from either a single or a set of blurred images. This can still be achieved with a poorly determined or unknown PSF. In blind deconvolution techniques, the PSF is estimated from the image or image set, allowing the deconvolution to be performed.

Blind deconvolution can be performed iteratively, where each iteration improves the estimation of the PSF and the scene, as in the case of MAP Estimation. It can also be performed non-iteratively like the APEX algorithm, where the algorithm, based on exterior information, extracts the PSF. Beginning with a good estimate of the PSF is helpful for quicker convergence but is not necessary to recover the target scene.

4

2.2 Optical Transfer Function

2.2.1 Average Short-Exposure OTF.   The average short-exposure OTF can be achieved by either of two methods. The first method involves averaging several short-exposure images together. The second requires that the tilt from several long-exposure images is removed before they are averaged. Short exposure images are created by integrating light from the target where the integration time does not exceed $\frac{1}{100}$ second [8]. The form of the equation for the short exposure transfer function can be seen here in (1).

$$\bar{H}_S(v) = exp\left\{-3.44\left(\frac{\bar{\lambda}fv}{R_0}\right)^{5/3}\left[1-\alpha\left(\frac{\bar{\lambda}fv}{D_0}\right)^{1/3}\right]\right\} \tag{1}$$

where α takes on the value unity for "near-field" and $\frac{1}{2}$ for "far-field" propagation. $\bar{\lambda}$ is the wavelength of the light, v is its frequency and f is the focal length of the imaging system. R_0 is the atmospheric seeing parameter and D_0 is the diameter of the optical system. When α is set to zero, the equation takes on the form of the long-exposure OTF, in (2).

The atmospheric coherence diameter R_0, also known as the seeing parameter first introduced by Fried [8], describes the image-degrading effects of the atmosphere. Typical values of R_0 at a mountain-top observatory might range from 5 cm under poor visibility up to 20 cm under exceptional viewing conditions.

2.2.2 Long-Exposure OTF.   Long exposure differs from short exposure with respect to the integration time used. Long exposure images typically use integration times much greater than $\frac{1}{100}$ second. This increased integration time also introduces wavefront tilt or wavefront fluctuations caused by the atmospheric winds [8]. The equation for the long exposure transfer function can be seen here in (2).

$$\bar{H}_L(v) \ = \ exp\left\{-3.44\left(\frac{\bar{\lambda}fv}{R_0}\right)^{5/3}\right\} \tag{2}$$

2.3   Statistics

The two statistics that are necessary for this thesis are the mean and variance of a dataset. The mean or average value is used to determine the signal to noise ratio to see if it is sufficient for this method to be able to converge properly.

2.3.1   Mean.   The mean of a random variable is equal to its average or expected value. The mean of the images used in this thesis is derived by summing each pixel value in the image and dividing that total by the number of pixels present.

$$Mean(X) \; = \; E\left[X\right] \; = \; \frac{1}{N}\sum_{i=1}^{N}X_i \tag{3}$$

where X represents any random variable and $E[\cdot]$ represents the expected value operator.

2.3.2   Variance.   The variance of a random variable is equal to the mean of the squared deviation of that variable from its expected value. The variance is, therefore, a measurement of how much fluctuation exists within the values of that variable. Likewise, the variance of the images can be determined by first finding the mean or average pixel value, as described above. Next subtract the mean from each of the pixel values and square the result. Next sum up all these results and divide by the number of pixels to determine the average variance of the scene.

$$Var(X) \; = \; E\left[(X - E[x])^2\right] \; = \; \frac{1}{N}\sum_{i=1}^{N}(X_i - \mu)^2 \tag{4}$$

where X represents any random variable, $(X - E[x])$ is the deviation and μ is the mean as in (3).

2.4 Signal To Noise Ratio

Signal to noise ratio (SNR) refers to the measure of a signal's strength relative to any background noise. If the SNR in question is not particularly strong (i.e. - orders of magnitude), then it may be to difficult to properly isolate the signal from the noise floor. SNR is typically represented as a ratio of either power or amplitude of a signal with respect to the noise.

$$SNR \;=\; \frac{P_{signal}}{P_{noise}} = \left(\frac{A_{signal}}{A_{noise}}\right)^2 \tag{5}$$

where P_{signal} represents the power of the signal, P_{noise} is the power of the noise level, A_{signal} is the amplitude of the signal, and A_{noise} is the amplitude of the noise level. Throughout this research and the simulations, SNR will be referred to as a ratio of amplitudes squared.

2.5 Types Of Noise and Their Distributions

The three main types of noise distributions that will be examined in this paper are Poisson, Gaussian, and negative binomial. Each noise type is dependent upon either the sensor configuration or the source of the target.

2.5.1 Gaussian.   The probability density function (pdf) for a continuous Gaussian distributed random variable x is [9]

$$f_X(x) \;=\; \frac{1}{\sqrt{2\pi}\sigma}e^{-(x-m)^2/2\sigma^2} \quad -\infty < x < \infty, \; \sigma > 0 \tag{6}$$

where m is the mean and σ is the variance.
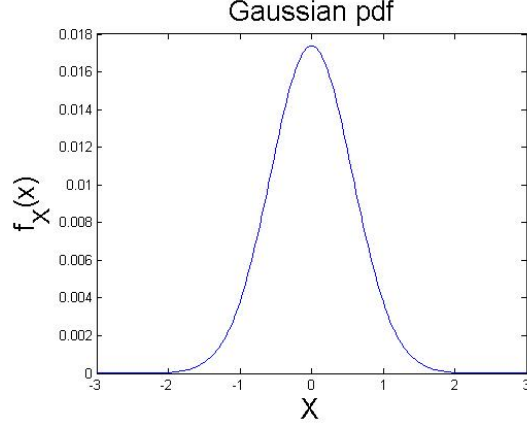
Figure 1: Gaussian distribution with mean = 0 and variance = 1.

When the majority of the noise is contributed by heat or electron leakage of the imaging system, the noise leans toward a Gaussian distribution. A charge-coupled device (CCD) is a device for the movement of electrical charges. It is in these CCD arrays of imaging systems where heat transfer and electron leakage is likely to occur. In this case, because the frequency spectrum is continuous and uniform for all frequency bands, the term white noise is used. Additive white Gaussian noise is the most common type of noise model used in electronic systems [6].

2.5.2   Poisson.   The probability mass function (pmf) for a discrete Poisson distributed random variable x is [9]

$$P[X = k] \equiv p_k \quad = \quad \frac{\alpha^k}{k!}e^{-\alpha}, \quad k = 0, 1, ..., \ \alpha > 0 \tag{7}$$

where α is the mean and the variance.
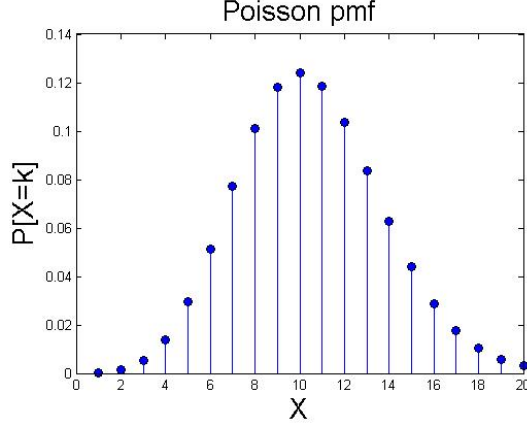
Figure 2: Poisson distribution with mean and variance $\alpha = 10.5$.

The noise tends to have a Poisson distribution when the dominant source of noise comes from the target when the target is being imaged from a passive system. As a general rule, photons impinging on a surface arrive in a random fashion after being reflected from various surfaces. Even though the average number of photons arriving per second is constant, the actual number for any given second can vary considerably. Therefore this noise, often referred to as shot noise, is modeled with a Poisson distribution [12].

2.5.3 Negative Binomial. The pmf for a discrete negative binomial distributed random variable x is [9]

$$P[X = k] \equiv p_k = \binom{k-1}{r-1} p^r (1-p)^{k-r}, \quad k = r, r+1, ... \tag{8}$$

where r is a positive number representing the number of successes in the same number of independent Bernoulli trials and p is the probability of success. For example, $r = 5$ refers to 5 successes in 5 independent trials.
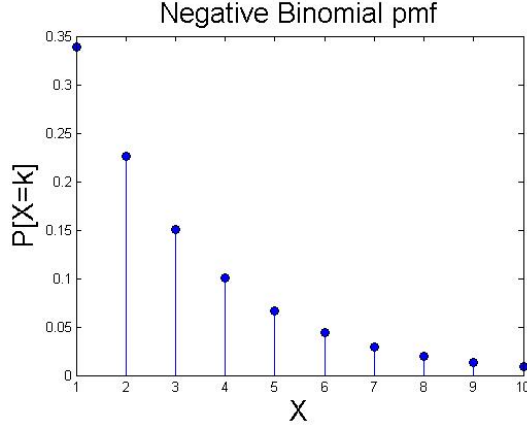
Figure 3: Negative binomial distribution with probability $p = 0.4$ and r represents 10 independent Bernoulli trials.

Data collected from active imagers, such as Light Detection and Ranging (LIDAR) systems, appear to have a negative binomial distribution caused by laser speckle resulting from the mutual interference of sets of wavefronts acting both constructively and destructively. The waves of light from the laser are coherent before they encounter the target. Since most targets are not perfectly flat, the returning laser pulses are no longer in phase. This means that the crests and troughs of the waves no longer line up with each light pulse. The scattered waves now interfere constructively to make bright points and destructively to make dark points. This light and dark pattern is referred to as laser speckle [2].

2.6   Richardson-Lucy Algorithm

The Richardson-Lucy algorithm is an iterative deconvolution method for recovering an image that has been blurred by a known point spread function [7]. The image estimate is updated upon each iteration of the algorithm.

$$d_i = \sum_j p_{ij} u_j \tag{9}$$

10

The objective is to determine the most likely image estimate, $\hat{u}_j$, given the observed image, d_i, and known PSF, p_{ij}, where $\hat{u}$ is an estimate of u. This leads to an equation for $\hat{u}_j$ which can be solved iteratively according to

$$\hat{u}_j^{t+1} = \hat{u}_j^t \sum_i \frac{d_i}{c_i} p_{ij} \tag{10}$$

where

$$c_i = \sum_j p_{ij} \hat{u}_j^t \tag{11}$$

It has been demonstrated that if this iteration converges, it will converge to the maximum likelihood solution [7].

2.7 Related Work

While there is much research in the area of blind deconvolution of astronomical data, most researchers are trying to solve the problem using the short exposure atmospheric model which negates phase delays due to atmospheric tilt [8]. This research, however, will examine the effects of both the long and short exposure optical transfer functions (OTFs). The diagram below is a visual depiction of what is going on when imaging an object through our atmosphere. Equations in following subsections explain the math behind the diagram.
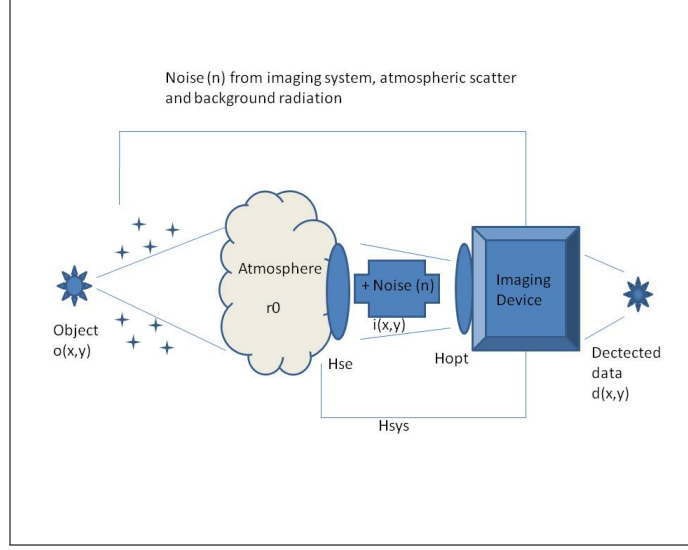
Figure 4: Astronomical imaging diagram

2.7.1 MAP Estimation. The MAP estimation method in [4] uses an iterative optimization approach along with a prior distribution over the quantity being estimated, to determine the estimate of the scene that maximizes the likelihood of it matching the true scene. The iterative approach of the MAP estimation algorithm researched for this paper relied on the average short exposure transfer function, below, to model the atmospheric effects.

$$\bar{H}_S(v) = exp\left\{-3.44\left(\frac{\bar{\lambda}fv}{R_0}\right)^{5/3}\left[1 - \alpha\left(\frac{\bar{\lambda}fv}{D_0}\right)^{1/3}\right]\right\} \tag{12}$$

The average OTF of the combined optical system and atmosphere, $\bar{H}_{sys}$, used in this paper, can be modeled by

$$\bar{H}_{sys}(x,y) \quad = \quad H_{opt}(x,y)\bar{H}_S(x,y) \tag{13}$$

where H_{opt} is the OTF of just the optical system and $\bar{H}_S$ is the short exposure OTF described by equation (12).

A pixel of the noisy blurred image may be expressed as the discrete convolution of $\bar{H}_{sys}$ with the remote scene, $o(x, y)$

$$i(x, y) = \bar{H}_{sys}(x, y)o(x, y)$$

The probability of the detected image pixel $d(x, y)$ given a particular observed remote scene pixel $o(x, y)$ can be described by (14). The probabilities are determined by the the data distributions as seen in Section 2.5. This particular probability has a negative binomial distribution.

$$P[d(x, y) = D(x, y)|o(x, y) = O(x, y)]$$

$$= \frac{(d(x, y) + M)!}{(d(x, y) + 1)!M!} \left(1 + \frac{M}{i(x, y)}\right)^{-d(x,y)} \left(1 + \frac{i(x, y)}{M}\right)^{-M} \tag{14}$$

where o is the estimate of the target object for a single iteration, M is the coherence parameter of the laser light, $d(x, y)$ represents the detected image and $i(x, y)$ is the added noise data [4].

$$f_{R_0}(R_0) = \left[\frac{e^{-N^2(R_0/r_{avg})}}{r_{avg}/N^2}\right] \tag{15}$$

is the assumed probability density function of the a posteriori data based on observation. N^2 is a scaling parameter and is equal to the number of pixels in the image. R_0 is the seeing parameter and r_{avg} represents the average value of R_0 [4].

It is from taking the log of the sum of equations (14) and (15) that the total log likelihood function [4] is formed:

$$L(o, R_0) = \Sigma_{x=1}^{N}\Sigma_{y=1}^{N}\left[\ln\left(\frac{(d(x, y) + M)!}{(d(x, y) + 1)!M!}\right) - d(x, y) \times\right.$$

13

$$\left(1 + \frac{M}{i(x,y)}\right) - Mln\left(1 + \frac{i(x,y)}{M}\right)\right] + ln[f_{R_0}(R_0)] \tag{16}$$

It can be shown that the likelihood function [4] reduces to

$$L(o, R_0) = \Sigma_{x=1}^{N}\Sigma_{y=1}^{N}\left(d(x,y)ln[i(x,y] - [d(x,y) + M] \times\right.$$

$$\left. ln[i(x,y) + M]\right) - N^2\frac{r_0}{r_{avg}} - ln\left[\frac{r_{avg}}{N^2}\right] \tag{17}$$

The maximization step [4] in which the derivative of $L(o, R_0)$ with respect to o is taken and set to zero, yields the following

$$\Sigma_{x=1}^{N}\Sigma_{y=1}^{N}\left(\frac{d(x,y)}{i(x,y)}\right)\bar{h}_{sys}(\xi - x, \eta - y) =$$

$$\Sigma_{x=1}^{N}\Sigma_{y=1}^{N}\left(\frac{d(x,y) + M}{M + i(x,y)}\right)\bar{h}_{sys}(x - \xi, y - \eta) \tag{18}$$

An update equation [4] can now be formed for the seeing parameter, similar to the Richardson-Lucy approach.

$$o^{new}(R_0) = o^{old}(R_0)\frac{\Sigma_{x=1}^{N}\Sigma_{y=1}^{N}\left(\frac{d(x,y)}{i(x,y)}\right)\bar{h}_{sys}(\xi - x, \eta - y)}{\Sigma_{x=1}^{N}\Sigma_{y=1}^{N}\left(\frac{d(x,y)+M}{M+i(x,y)}\right)\bar{h}_{sys}(x - \xi, y - \eta)} \tag{19}$$

where
$$i(x,y) = i^{old}(x,y) = \Sigma_{\xi=1}^{N}\Sigma_{\eta=1}^{N}\bar{h}_{sys}(x - \xi, y - \eta)o^{old}(\xi, \eta) \tag{20}$$

The MAP estimation [4] now becomes

$$o^{new}(R_0) = o^{old}(R_0)\frac{\Sigma_{x=1}^{N}\Sigma_{y=1}^{N}\left(\frac{d(x,y)}{i^{old}(x,y)}\right)\bar{h}_{sys}(x - \xi, y - \eta)}{\Sigma_{x=1}^{N}\Sigma_{y=1}^{N}\bar{h}_{sys}(x - \xi, y - \eta)} \tag{21}$$

2.7.2 APEX. The APEX method [5] is a general solution to a specific limited class of blur. In order for the technique to be effective, the blur must be

symmetric along with certain other mathematical characteristics. APEX is based on a major simplifying assumption instead of an iterative approach. It's fast and it does not need to know the PSF because the algorithm calculates it directly from the image. The equation for calculating the PSF directly from the image is

$$
\begin{aligned}
h(\xi, \eta) &= \int_{R^2} h(x, y) e^{[-2\pi i(\xi x + \eta y)] dx dy} \\
&= e^{-\alpha(\xi^2 + \eta^2)^\beta}, \ 0 \le \alpha \le 1, \ 0 < \beta \le 1
\end{aligned}
\tag{22}
$$

where the α and β values are determined by the the specific application of the blurring function. For example, medical imagery and astronomical imagery would use different values for α and β to sharpen the image. It does require prior knowledge of these α and β values used to blur the image. For example, the diffraction-limited optical transfer function (OTF) for a perfect lens can be approximated with $\beta = \frac{3}{4}$ and where α is a function of the cutoff frequency. For long-exposure imaging through atmospheric turbulence, $\beta = \frac{5}{6}$ and α values are determined by atmospheric conditions [8].

2.7.3 Results. The following sets of images in Figures 5 and 6 show how the MAP estimation technique works on a fully illuminated scene of a courtyard. Fully-illuminated refers to the fact that a majority of the pixels in the image have a value greater than zero and are discernible against a black background.

15

(a)   (b)

Figure 5: (a) is the truth data and shows the scene of the courtyard before any distortion. (b) shows the scene with with blurring applied. The R_0 value of the simulated atmosphere is 10 cm and plot of the OTF can be seen in the Figure 6.
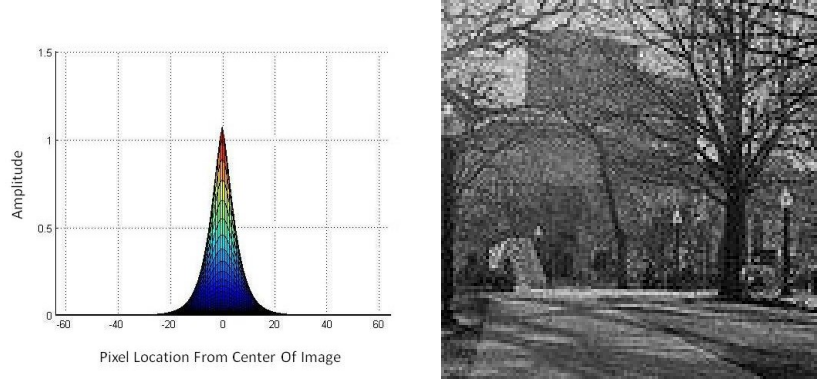
(a)   (b)

Figure 6: (a) shows the side-view of the OTF that was convolved with the courtyard image to cause the blur. (b) depicts the recovered scene from the blurred image after 1000 iterations of the MAP estimator.

Now that this method has been shown to have satisfactory results using fully illuminated scenes, let's examine its ability to accurately estimate the seeing parameter on astronomical datasets.

(a)   (b)
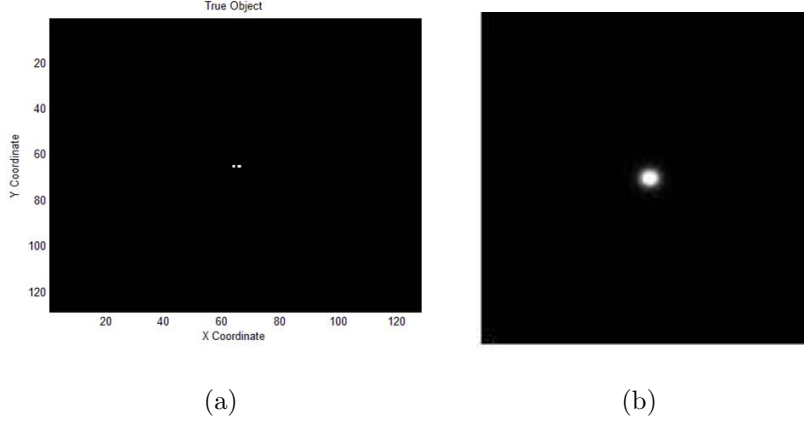
Figure 7: (a) shows what the binary star data looks like without any blur. The stars are separated from each other by 1 pixel. (b) shows the same binary stars blurred with the same OTF in Figure 6.
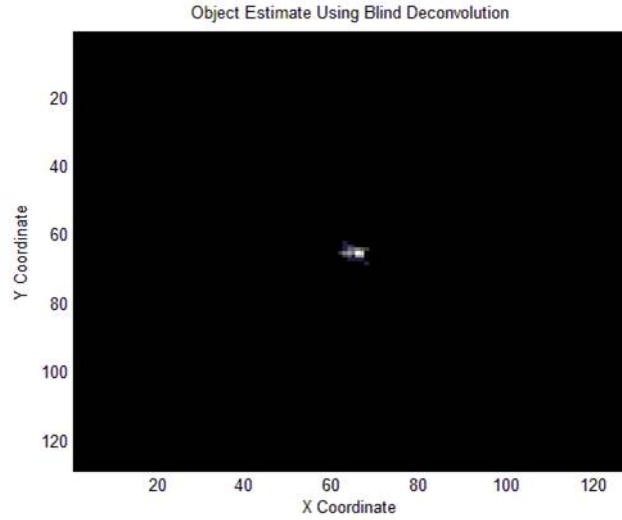
Figure 8: This image shows the difficulty that the MAP Estimation algorithm had while trying to recover the scene.

The difficulty the MAP estimator has while processing sparse data can be seen in the image above. It is due to the way the a posteriori information is used. Recall the N^2 scaling factor from equation (15). It turns out that this scaling factor, based on the number of pixels in the scene, is only accurate for fully illuminated scenes. In the case of astronomical data sets where the actual data is sparse, the scaling

factor drives the a posteriori data to zero, making it useless. This can be seen in the following image.
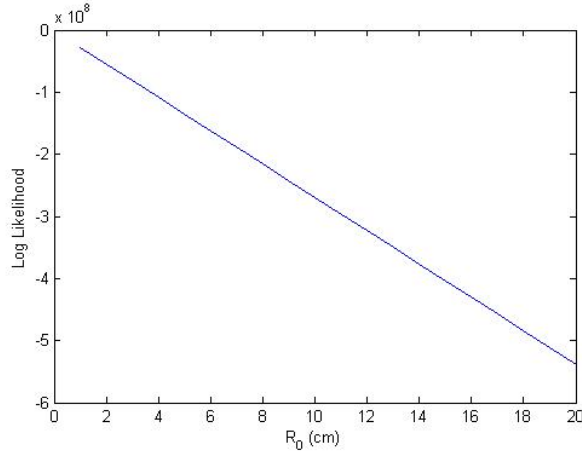
Figure 9: This image shows the difficulty that the MAP Estimation algorithm had while trying to recover the scene. This plot shows that the log-likelihood value which is way off from the 10 cm that it should be. Here the weighting factor, N^2 is set to the number of pixels in the scene, $16,384$.

The next two images in figures 10 and 11 show how varying the value of N can result in better estimations. The correct value for R_0 is 10 cm and is somewhere between the estimates seen in these examples. The first guess of using a scaling factor of 10 does not plateau but seems to increase asymptotically. The next guess of 50 causes the estimator to converge prematurely. One can obtain the correct value of R_0 by messing with these settings manually over a period of trial and error. However, these results are image dependent and are not a viable means for automatic estimation.
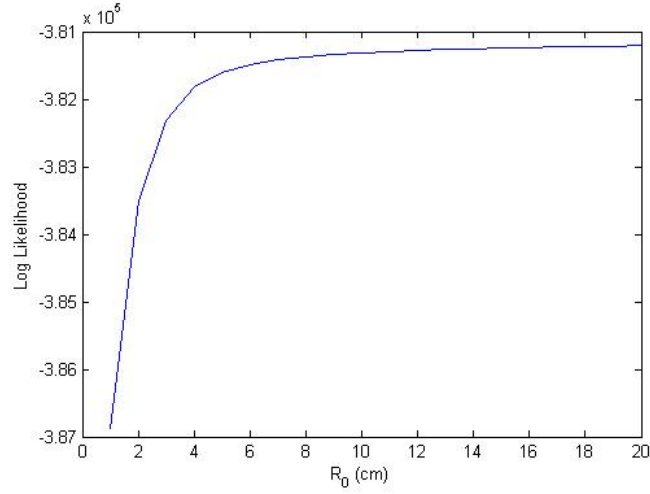
Figure 10: This image shows result of the MAP Estimation algorithm when N was set to 10.
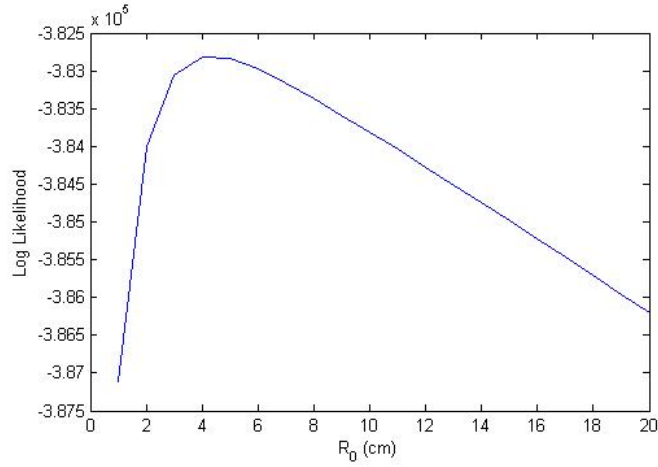
Figure 11: This image shows result of the MAP Estimation algorithm when N was set to 50.

The APEX method is not without its own difficulties when dealing with astronomical data. Figures 12 and 13 demonstrate how varying the space between the stars has a drastic effect on the ability of the algorithm to accurately estimate R_0. Figures 12 and 13 take the row of interest containing the binary stars and perform a Fourier transform to examine the spatial frequency content. Next they compare the amplitude of the spatial frequencies to the result of the APEX algorithm.
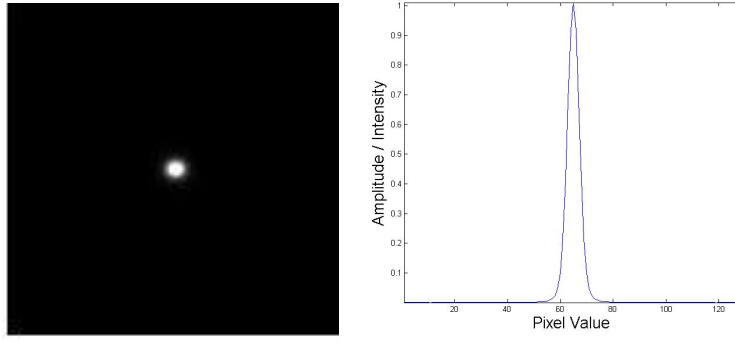
(a)

(b)
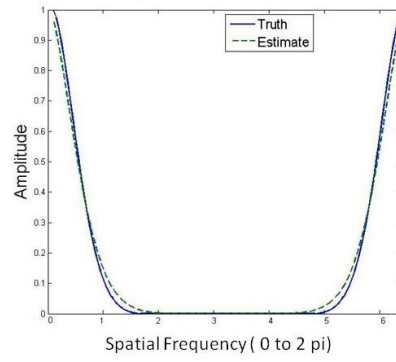
(c)

Figure 12: (a) shows the blurry image of a binary star pair separated by one pixel (b) is the result of taking a slice of the image through the binary stars and plotting its amplitude (c) shows the result of taking the Fourier transform of the data (subfigure b) and applying the APEX algorithm. Both the spatial frequency of the true data and the APEX estimation are shown for comparison.

(a)   (b)

(c)
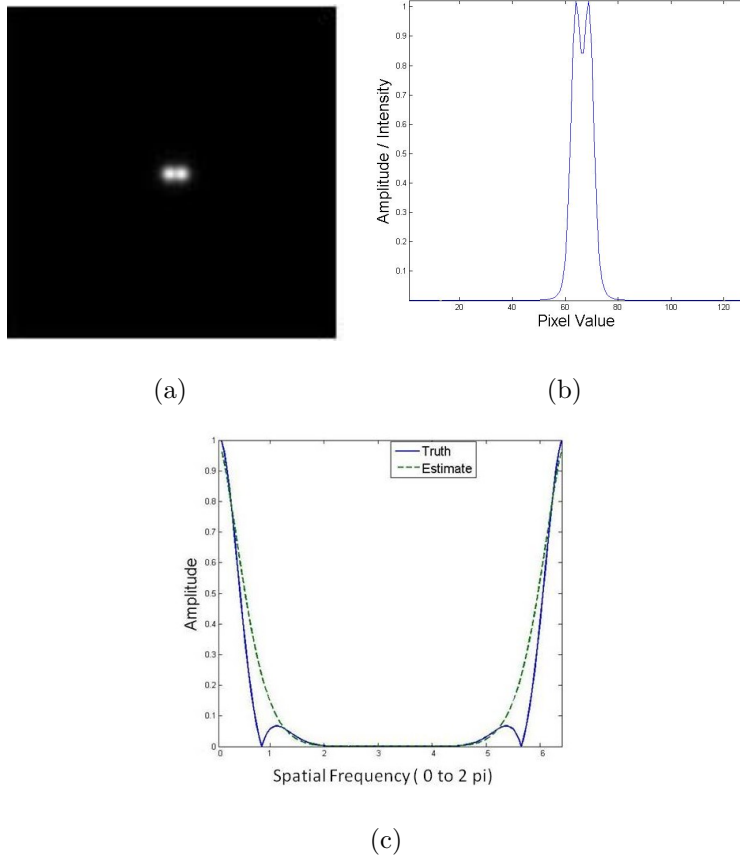
Figure 13: (a) shows the blurry image of a binary star pair separated by four pixels (b) is the result of taking a slice of the image through the binary stars and plotting its amplitude (c) shows the result of taking the Fourier transform of the data (subfigure b) and applying the APEX algorithm. Both the spatial frequency of the true data and the APEX estimation are shown for comparison.

The estimation in Figure 12 was accurate but it already started to deviate from the truth data by the time the stars were separated by three pixels, as seen in Figure 13. This is due to the fact that objects really close to one another appear as a single point source. As soon as the separation becomes apparent to the APEX algorithm, it has difficulty with multiple point sources.

MAP estimation was demonstrated on fully illuminated photographs and both the MAP estimation and APEX blind deconvolution methods were applied to as-

21

tronomical data sets. These simulations, both with full-scene and sparse datasets, looked at only one particular optical system. The telescope receiver aperture was 20 centimeters and an atmospheric seeing parameter of 10 centimeters was assumed. In this particular case, the MAP estimation performed well on photographic images. However, both methods were shown not to be reliable when estimating astronomical data sets, each for their own reasons.

MAP estimation wasn't accurate because the scaling factor of the a posteriori calculation fails in the absence of fully illuminated data. As soon as there appear to be more than one point source, the APEX method breaks down as well. It's for these reasons that the two methods explored in this chapter are not an effective means for deblurring astronomical data.

Instead, Chapter III proposes a new technique in which no information about the point spread function or seeing parameter is needed. This is the usual case when dealing with astronomical data. The proposed research effort would attempt to develop a blind deconvolution method that produces useful results when processing astronomical scenes. The new technique will compare the statistics of a blurry image to an estimate of the actual image, in an iterative approach, in order to determine the true atmospheric seeing parameter.

III.   Research Methodology

This chapter deals with the convergence of variance method. It briefly details the approach below to improve upon current work in the area of blind deconvolution. Next, the expectation maximization steps are discussed and derivations for both the Poisson and Gaussian noise cases are provided. Next the coarse and fine search approach to finding the best estimated R_0 is discussed. Finally, the areas of interest which were covered under this research for the convergence of variance method are discussed. Example data results for these areas are provided in chapter 4. These areas include the effect of SNR, sparsity of the scene, varying seeing parameter values, and exposure type.

3.1   Convergence of Variance Method

The convergence of variance (COV) method that was developed for this research has two main parts. The first part of this method involves deriving the expectation maximization equations needed for a particular noise distribution of the data. This will allow for the correct estimations of the images to be made. The next part of this method involves using the variance of the observed image as the stopping criteria for the expectation maximization algorithm.

The first step is to acquire an astronomical image and compute its variance. Next, in an iterative Richardson-Lucy approach, the variance of the observed image and the variance of the latest estimate of the image are compared. However, unlike in the Richardson-Lucy approach, here the PSF does not need to be known. For the first estimate, the seeing parameter estimate is set equal to 1. This process will continue until the length of the iterations, needed to converge, reaches a predetermined threshold set by the image analyst. Once, this threshold is met, the value of the seeing parameter estimate is incremented and the process repeats. Once the variance of the image estimate converges with the variance of the acquired astronomical image, the best estimate of the seeing parameter is known and the image can be seen as it would appear without the blurring effects of the atmosphere.

3.2 Expectation Maximization (EM) Algorithm

An EM algorithm is widely used in the iterative calculations of maximum likelihood estimates. The EM algorithm is not a single algorithm but rather a framework or approach to solving a problem [3]. During each iteration or estimate refinement, the EM algorithm goes through both an expectation and a maximization step. The initial values or parameters are estimated iteratively until convergence. Other good sources for papers which use an EM approach to blind deconvolution can be found in [1, 4, 10, 11]. The EM derivations for images containing Gaussian and Poisson random variables are included below. An example of EM, using negative-binomial random variables, is found in Chapter 2 Section 7.1, MAP estimation.

3.2.1 EM Steps.   Here are the main steps in the EM process. These steps are outlined below in each of the derivations.

1. Obtain statistical model for the measured (incomplete) data, d

2. Obtain statistical model for the complete data, $\tilde{d}$

3. Formulate the complete data log-likelihood, L

4. Compute expectation step

5. Compute maximization step

6. Compute update equation

3.2.2 Poisson EM Derivation.

Step 1: Obtain statistical model for the measured data:

$$
\begin{aligned}
E\left[d(x,y)\right] &= i(x,y) = \sum_{z,w=1}^{N} o(z,w)h(x-z,w-y) \\
P\left[d(x,y)\right] &= \frac{i(x,y)^{d(x,y)}e^{-i(x,y)}}{d(x,y)!}
\end{aligned}
\tag{23}
$$

The measured data is an image in which each pixel is a realization of a Poisson random variable whose mean is the result of a convolution. h is a linear operator that

transforms the true image, o, into the mean of the noisy blurred image, i.

Step 2: The complete data: Invent a set of mythical (complete) data, $\tilde{d}$ and a relationship between this set and the measured (incomplete) data, d. We choose the complete data to be related to the incomplete data through equation (24).

$$d(x, y) \;=\; \sum_{z,w} \tilde{d}(x, y, z, w) \tag{24}$$

Statistical model for the complete data: Select a statistical model for the complete data such that it produces the statistical model for the incomplete data through their defined relationship. We chose the complete data to be Poisson as well since the sum of Poisson random variables is also Poisson.

$$
\begin{aligned}
E\left[\tilde{d}(x, y, z, w)\right] &= o(z, w)h(x - z, y - w) \\
E\left[\sum_{z,w} \tilde{d}(x, y, z, w)\right] &= \sum_{z,w} E\left[\tilde{d}(x, y, z, w)\right] \\
\sum_{z,w} o(z, w)h(x - z, y - w) &= E\left[d(x, y)\right]
\end{aligned}
\tag{25}
$$

Step 3: Formulate the complete data log-likelihood:

$$P\left[\tilde{d}(x,y,z,w)\right] = \frac{o(z,w)h(x-z,y-w)^{\tilde{d}(x,y,z,w)}e^{-o(z,w)h(x-z,y-w)}}{\tilde{d}(x,y,z,w)!}$$

$$\underline{\tilde{\mathbf{d}}} = \tilde{d}(x,y,z,w)\forall(x,y,z,w)\in I(1,N)$$

$$P\left[\underline{\tilde{\mathbf{d}}}\right] = \prod_{x,y,z,w=1}^{N}\frac{o(z,w)h(x-z,y-w)^{\tilde{d}(x,y,z,w)}e^{-o(z,w)h(x-z,y-w)}}{\tilde{d}(x,y,z,w)!}$$

$$L(o,h) = \ln\left(P\left[\tilde{d}(x,y,z,w)\forall(x,y,z,w)\in I(1,N)\right]\right)$$

$$= \sum_{x,y,z,w=1}^{N}\tilde{d}(x,y,z,w)\ln(o(z,w)h(x-z,y-w))$$

$$- o(z,w)h(x-z,y-w)-\ln(\tilde{d}(x,y,z,w)!) \tag{26}$$

Step 4: Find the expected value of the complete data log-likelihood.

$$E\left[L(o,h)|d(x,y),o^{old},h\right] = Q(o,h)$$

$$= \sum_{x,y,z,w}E\left[\tilde{d}(x,y,z,w)|d(x,y),o^{old},h\right]$$

$$* \quad [\ln(o(z,w)h(x-z,y-w))]-o(z,w)h(x-z,y-w)$$

$$- E\left[\ln(\tilde{d}(x,y,z,w)!|d(x,y),o^{old}\right] \tag{27}$$

Define two statistically independent Poisson variables that adhere to the relationship defined in (24).

$$d_1 = \tilde{d}(x,y,z_0,w_0)d_2$$

$$= \sum_{z,w}\tilde{d}(x,y,z,w)-\tilde{d}(x,y,z_0,w_0) \tag{28}$$

Define the expected value and probability of Poisson randomly distributed datasets. Here is the simple case of two arbitrary Poisson variables. It's easier to determine

the probability when summing two Poisson variables, than it would be for a Poisson variable for each pixel in the scene. Since the sum of Poissons is also Poisson, this case can be extented to n Poisson variables.

$$
\begin{aligned}
E[d_1] &= m_1 \\
E[d_2] &= m_2 \\
d(x,y) &= d = d_1 + d_2 \\
P[d_1, d_2] &= \frac{m_1^{d_1} e^{-m_1}}{d_1!} \frac{m_2^{d_2} e^{-m_2}}{d_2!}, \quad d_1, d2 = 0, 1, 2, ... \\
d_2 &= d - d_1 \\
P[d, d_1] &= \frac{m_1^{d_1} e^{-m_1}}{d_1!} \frac{m_2^{(d-d_1)} e^{-m_2}}{(d - d_1)!}
\end{aligned}
\tag{29}
$$

Next, find the probability of the complete data given the measured dataset. This is the case in which each pixel is a Poisson random variable and $\tilde{d}$ is the sum of all variables.

$$
\begin{aligned}
P[d_1|d] &= P[d, d_1]/P[d] \\
&= (d!)\frac{m_1^{d_1} e^{-m_1}}{d_1!} \frac{m_2^{(d-d_1)} e^{-m_2}}{(d - d_1)!} / [(m_1 + m_2)^d e^{-(m_1+m_2)}] \\
P[d_1|d] &= \frac{(d!)m_1^{d_1}}{(m_1 + m_2)^d d_1!} \frac{m_2^{(d-d_1)}}{(d - d_1)} \\
&= \frac{(d!)m_1^{d_1}}{(m_1 + m_2)^{(d_1+d-d_1)} d_1!} \frac{m_2^{(d-d_1)}}{(d - d_1)!} \\
P[d_1|d] &= \frac{(d!)(m_1/[m_1 + m_2])^{d_1}}{d_1!} \frac{(m_2/[m_1 + m_2])^{(d-d_1)}}{(d - d_1)!} \\
E[d_1|d] &= d(m_1/[m_1 + m_2])
\end{aligned}
\tag{30}
$$

$$
E\left[\tilde{d}(x,y,z,w)|d(x,y), o^{old}, h\right] = \frac{d(x,y)o^{old}(z,w)h(x - z, y - w)}{i^{old}(x,y)}
\tag{31}
$$

Now substitute (31) into Q(o,h) from (27).

$$
\begin{aligned}
Q(o, h) \;=\; & \sum_{x,y,z,w} \left(\frac{d(x,y)o^{old}(z,w)h(x-z,y-w)}{i^{old}(x,y)} \right. \\
& * \quad [\ln(o(z,w)h(x-z,y-w))] - o(z,w)h(x-z,y-w) \\
& - \quad \left. E[\ln(\tilde{d}(x,y,z,w)!)|d(x,y,o)^{old}, h] \right)
\end{aligned}
\tag{32}
$$

Step 5: Maximize the result by first taking the derivative and then setting it equal to zero. The variables z_0 and w_0 are specific locations of the generic variables, z and w.

$$
\begin{aligned}
\frac{\partial Q(o,h)}{\partial o(z_0, w_0)} \;=\; & \sum_{x,y,z,w} \left(\frac{\partial}{\partial o(z_0, w_0)} \right. \\
& * \quad \frac{d(x,y)o^{old}(z,w)h(x-z,y-w)}{i^{old}(x,y)} \ln(o(z,w)h(x-z,y-w)) \\
& - \quad \frac{\partial}{\partial o(z_0, w_0)} o(z,w)h(x-z,y-w) \\
& - \quad \left. \frac{\partial}{\partial o(z_0, w_0)} E[\ln(\tilde{d}(x,y,z,w)!)|d(x,y)o^{old}] \right)
\end{aligned}
\tag{33}
$$

Now that the derivative has been taken, most terms go away and the remaining term is set equal to zero

$$
0 \;=\; \sum_{x,y,z,w} \frac{\partial}{\partial o(z_0, w_0)} E[\ln(\tilde{d}(x,y,z,w)!)|d(x,y)o^{old}]
$$

$$
\frac{\partial}{\partial o(z_0, w_0)} o(z,w)h(x-z,y-w) \;=\; \delta(z-z_0, w-w_0)h(x-z,y-w)
$$

$$\frac{\partial}{\partial o(z_0, w_0)} \quad * \quad \frac{d(x,y)o^{old}(z,w)h(x-z,y-w)}{i^{old}(x,y)}$$
$$* \quad [\ln(o(z,w)h(x-z,y-w))]$$
$$= \quad \frac{d(x,y)o^{old}(z,w)h(x-z,y-w)}{i^{old}(x,y)} \frac{\partial}{\partial o(z_0,w_0)} \ln(o(z,w))$$
$$= \quad \frac{d(x,y)o^{old}(z,w)h(x-z,y-w)}{i^{old}(x,y)} \frac{1}{\partial o(z,w)} \frac{\partial o(z,w)}{\partial o(z_0,w_0)}$$
$$= \quad \frac{d(x,y)o^{old}(z,w)h(x-z,y-w)}{i^{old}(x,y)} \frac{1}{\partial o(z,w)} \delta(z-z_0, w-w_0)$$

$$(34)$$

Maximize Q with respect to $h(z_0, w_0)$.

$$\frac{\partial Q(o,h)}{\partial h(z_0,w_0)} = \sum_{x,y,z,w} \frac{d(x,y)o^{old}(z,w)h(x-z,y-w)}{i^{old}(x,y)}$$
$$* \quad \left[\frac{\delta(x-z-z_0, y-w-w_0)}{h(x-z,y-w)} \right] - \delta(x-z-z_0, y-w-w_0)o(z,w)$$

$$(35)$$

Now, apply the sifting property of the Dirac function:

$$\frac{\partial Q(o,h)}{\partial h(z_0,w_0)} = \sum_{x,y} \frac{d(x,y)o^{old}(z,w)h(x-z,y-w)}{i^{old}(x,y)} \frac{1}{h(z_0,w_0)} - o(x-z_0, y-w_0)$$
$$\frac{\partial Q(o,h)}{\partial h(z_0,w_0)} = 0$$
$$0 = \sum_{x,y} \frac{d(x,y)o^{old}(z,w)h(x-z,y-w)}{i^{old}(x,y)} \frac{1}{h(z_0,w_0)} - o(x-z_0, y-w_0)$$

$$(36)$$

Find the new estimate for the object

$$\sum_{x,y} o(x - z_0, y - w_0) = \sum_{x,y} \frac{d(x,y)o^{old}(z_0, w_0)h(x - z, y - w)}{i^{old}(x,y)} \frac{1}{h(z_0, w_0)}$$

$$h(z_0, w_0) = \frac{h(z_0, w_0) \sum_{x,y} \frac{d(x,y)o^{old}(z,w)h(x-z_0,y-w_0)}{i^{old}(x,y)}}{\sum_{x,y} o(x - z_0, y - w_0)}$$

$$o^{new}(z_0, w_0) = \frac{o^{old}(z_0, w_0) \sum_{x,y} \frac{d(x,y)h(x-z_0,y-w_0)}{i^{old}(x,y)}}{\sum_{x,y} h(x - z_0, y - w_0)} \qquad (37)$$

Step 6: Form the update equation for estimated object

We chose h summing to 1 to be a constraint since this will ensure the conservation of energy in the system. That is, both the true image and the estimated image would both contain the same number of photons.

$$Choose \sum_{x,y} h(x - z_0, y - w_0) = 1$$

$$\boxed{o^{new}(z_0, w_0) = o^{old}(z_0, w_0) \sum_{x,y} \frac{d(x,y)h(x - z_0, y - w_0)}{i^{old}(x,y)}} \qquad (38)$$

Show that the OTF update sums to 1

$$h(z_0, w_0) = \frac{h(z_0, w_0) \sum_{x,y} \frac{d(x,y)o^{old}(x-z_0,y-w_0)}{i^{old}(x,y)}}{\sum_{x,y} o(x - z_0, y - w_0)}$$

$$= \frac{h(z_0, w_0) \sum_{x,y} \frac{d(x,y)o^{old}(x-z_0,y-w_0)}{i^{old}(x,y)}}{\sum_{x,y} d(x,y)}$$

$$\sum_{x,y} h(z_0, w_0) = \frac{\sum_{x,y} h(z_0, w_0) \sum_{x,y} \frac{d(x,y)o^{old}(x-z_0,y-w_0)}{i^{old}(x,y)}}{\sum_{x,y} d(x,y)}$$

$$= \frac{\sum_{x,y} \frac{(x,y)}{i^{old}(x,y)} \sum_{x,y} o^{old}(x - z_0, y - w_0)h(z_0, w_0)}{\sum_{x,y} d(x,y)} \qquad (39)$$

$$i^{old}(x,y) = \sum_{x,y} o^{old}(x-z_0, y-w_0)h(z_0, w_0)$$

$$\sum_{x,y} h^{new}(z_0, w_0) = \frac{\sum_{x,y} d(x,y)}{\sum_{x,y} d(x,y)} = 1 \qquad (40)$$

3.2.3   Gaussian EM Derivation.

Step 1: Obtain statistical model for the measured data:

$$E[d(x,y)] = i(x,y) = \sum_{z,w=1}^{N} o(z,w)h(x-z, w-y)$$

$$P[d(x,y)] = \frac{1}{\sqrt{2\pi}\sigma} e^{\frac{(d(x,y)-i(x,y))^2}{2\sigma^2}} \qquad (41)$$

The measured data is an image in which each pixel is a realization of a Gaussian random variable whose mean is the result of a convolution. h is a linear operator that transforms the true image, o, into the mean of the noisy blurred image, i.

Step 2: The complete data: Invent a set of mythical (complete) data, $\tilde{d}$ and a relationship between this set and the measured (incomplete) data, d. We choose the complete data to be related to the incomplete data through equation (41).

$$d(x,y) = \sum_{z,w=1}^{N} \tilde{d}(x,y,z,w) \qquad (42)$$

Statistical model for the complete data: Select a statistical model for the complete data such that it produces the statistical model for the incomplete data through their defined relationship. We chose the complete data to be Gaussian as well since the sum of Gaussian random variables is also Gaussian.

31

$$
\begin{aligned}
E\left[\tilde{d}(x, y, z, w)\right] &= o(z, w)h(x - z, w - y) \\
P\left[\tilde{d}(x, y)\right] &= \frac{1}{\sqrt{2\pi}\sigma}e^{-\frac{(\tilde{d}(x,y,z,w) - o(z,w)h(x-z,w-y))^2}{2\sigma^2}}
\end{aligned}
\tag{43}
$$

Step 3: Formulate the complete data log-likelihood:

$$
\begin{aligned}
\underline{\tilde{\mathbf{d}}} &= \tilde{d}(x, y, z, w)\forall(x, y, z, w) \in I(1, N) \\
P\left[\underline{\tilde{\mathbf{d}}}\right] &= \prod_{x,y,z,w=1}^{N} \frac{1}{\sqrt{2\pi}\sigma}e^{-\frac{(\tilde{d}(x,y,z,w) - o(z,w)h(x-z,w-y))^2}{2\sigma^2}} \\
L(o, h) &= \ln\left(P\left[\tilde{d}(x, y, z, w)\forall(x, y, z, w) \in I(1, N)\right]\frac{1}{\sqrt{2\pi}\sigma}\right) \\
&= \sum_{x,y,z,w=1}^{N} \frac{(\tilde{d}(x, y, z, w) - o(z, w)h(x - z, w - y))^2}{2\sigma^2}\ln\left(\frac{1}{\sqrt{2\pi}\sigma}\right)
\end{aligned}
\tag{44}
$$

Step 4: Find the expected value of the log-likelihood.

$$
\begin{aligned}
Q(o) = E[L(o)|d(x, y), o_{old}(z, w)] &= \sum_{x,y,z,w}\left(- E[(\tilde{d}(x, y, z, w)|o_{old}(z, w), d(x, y))^2]\right. \\
&\quad + 2E[(\tilde{d}(x, y, z, w)|o_{old}(z, w), d(x, y))] \\
&\quad \left. + o(z, w)^2 h(x - z, y - w)^2\right)
\end{aligned}
\tag{45}
$$

Now find this piece of (46) by defining two sets of Gaussian random variables in (48).

$$
E\left[\tilde{d}(x, y, z, w)|d(x, y), o(z, w)\right]
\tag{46}
$$

First, the two sets of Gaussian randomly distributed data are defined below.

$$
\begin{aligned}
d &= d_1 + d_2 \\
d_1 &= \tilde{d}(x, y, z_0, w_0) \\
d_2 &= \sum_{z,w=1}^{N} \tilde{d}(x, y, z, w) - \tilde{d}(x, y, z_0, w_0)
\end{aligned}
\tag{47}
$$

The mean and variances for the complete data are provided below.

$$(48)$$

$$
\begin{aligned}
E[d_1] &= m_1,\ Var[d_1] = \sigma^2 \\
E[d_2] &= m_2,\ Var[d_2] = \sigma^2(n^2 - 1) \\
d(x, y) &= d = d_1 + d_2
\end{aligned}
$$

$$(49)$$

Now the probability of complete data is calculated

$$
\begin{aligned}
P[d_1, d_2] &= \frac{1}{\sqrt{2\pi}\sigma} exp\left(-\frac{(d_1 - m_1)^2}{2\sigma^2}\right) \frac{1}{\sigma\sqrt{2\pi(n^2-1)}} exp\left(-\frac{(d_2 - m_2)^2}{2\sigma^2(n^2-1)}\right) \\
P[d, d_1] &= \frac{1}{2\pi\sigma^2\sqrt{n^2-1}} exp\left(-\frac{(d_1 - m_1)^2}{2\sigma^2}\right) exp\left(-\frac{(d - d_1 - m_2)^2}{2\sigma^2(n^2-1)}\right)
\end{aligned}
$$

$$(50)$$

The probability of complete data can be determined, given the set of measured data

$$
\begin{aligned}
P[d_1|d] &= \frac{\frac{1}{2\pi\sigma^2\sqrt{n^2-1}} exp\left(-\frac{(d_1-m_1)^2}{2\sigma^2}\right) exp\left(-\frac{(d-d_1-m_2)^2}{2\sigma^2(n^2-1)}\right)}{\frac{1}{\sqrt{2\pi}\sigma n} exp\left(-\frac{(d-d_1-m_2)^2}{2\sigma^2 n^2}\right)} \\
P[d_1|d] &= \frac{\sqrt{2}n}{2\sigma\sqrt{\pi(n^2-1)}} exp\left(\frac{(d-d_1-m_2)^2}{2\sigma^2 n^2}\right) \\
&\quad * \ exp\left(-\frac{(d_1-m_1)^2}{2\sigma^2}\right) exp\left(-\frac{(d-d_1-m_2)^2}{2\sigma^2(n^2-1)}\right) \\
P[d_1|d] &= \frac{\sqrt{2}n}{2\sigma\sqrt{\pi(n^2-1)}} exp\left(-\frac{(n^2 d_1 - n^2 m_1 + m_2 + m_1 - d)^2}{2n^2\sigma^2(n^2-1)}\right) \\
P[d_1|d] &= \frac{\sqrt{2}n}{2\sigma\sqrt{\pi(n^2-1)}} exp\left(-\frac{\left(d_1 - \left(m_1 + \left(\frac{-m_2-m_1+d}{n^2}\right)\right)\right)^2}{\frac{2n^2\sigma^2(n^2-1)}{n^4}}\right) \\
E[d_1|d] &= m_1 + \frac{(d - m_1 - m_2)}{n^2}
\end{aligned}
$$

$$(51)$$

Substituting these results back into the previous form of the equation yields the following result.

$$
\begin{aligned}
E[\tilde{d}(x,y,z,w)|o_{old}(z,w),d(x,y)] &= o_{old}(z,w),h(x-z,y-w) \\
&+ \left(\frac{-(i_{old}(x,y)-o_{old}(z,w)h(x-z,y-w))}{n^2}\right) \\
&- \left(\frac{o_{old}(z,w)h(x-z,y-w)+d(x,y)}{n^2}\right) \\
&= o_{old}(z,w)h(x-z,y-w) + \frac{(d(x,y)i_{old}(x,y))}{n^2}
\end{aligned}
$$

$$(52)$$

Step 5: Maximize the result by taking the derivative and setting it equal to zero.

$$
\begin{aligned}
\frac{\partial Q(o)}{\partial o(z_0,w_0)} &= \sum_{x,y,z,w} \frac{\partial Q(o)}{\partial o(z_0,w_0)}\left(-E[(\tilde{d}(x,y,z,w)|o_{old}(z,w),d(x,y))^2]\right. \\
&+ 2E[(\tilde{d}(x,y,z,w)|o_{old}(z,w),d(x,y))]\frac{o(z,w)h(x-z,y-w)}{2\sigma^2} \\
&+ \left. o(z,w)^2 h(x-z,y-w)^2\right)
\end{aligned}
$$

$$(53)$$

Equation (55) is the first piece of (54) and doesn't depend on $o(z_0,w_0)$, so taking $\frac{\partial Q(o)}{\partial o(z_0,w_0)}$ and setting it equal to 0 yields:

$$
\sum_{x,y,z,w} \frac{\partial}{\partial o(z_0,w_0)}E[(\tilde{d}(x,y,z,w)|o_{old}(z,w),d(x,y))^2] = 0
$$

$$(54)$$

Equation (56) is the second piece of (54).

$$
\sum_{x,y,z,w} \frac{\partial}{\partial o(z_0,w_0)}\left[\frac{2o(z,w)h(x-z,y-w)}{2\sigma^2}*\right.
$$
$$
\left.\left(o_{old}(z,w)h(x-z,y-w)+\frac{(d(x,y)-i(x,y))}{n^2}\right)\right] =
$$

$$\sum_{x,y,z,w} \left[2o(z-z_0, w-w_0)h(x-z, y-w) * \right.$$

$$\left. \left(o_{old}(z,w)h(x-z, y-w) + \frac{(d(x,y) - i(x,y))}{n^2} \right) \right] =$$

$$\sum_{x,y} \left[2o_{old}(z,w)h(x-z_0, y-w_0)^2 + \right.$$

$$\left. \left(h(x-z_0, y-w_0) * \frac{(d(x,y) - i(x,y))}{n^2} \right) \right] = \tag{55}$$

Equation (57) is the third and final piece of (54).

$$\sum_{x,y,z,w} \left[\frac{\partial o(z,w)^2 h(x-z, y-w)^2}{\partial o(z_0, w_0)} \right] =$$

$$\sum_{x,y,z,w} \left[2\partial(z-z_0, w-w_0)o(z,w)h(x-z, y-w)^2 \right] =$$

$$\sum_{x,y} \left[2o(z_0, w_0)h(x-z_0, y-w_0)^2 \right] \tag{56}$$

Substituting the results of (55),(56), and (57)back into (54) yields:

$$0 = \frac{\partial Q(o)}{\partial o(z_0, w_0)} = \sum_{x,y} \frac{2o_{old}(z_0, w_0)h(x-z_0, y-w_0)^2}{2\sigma^2}$$

$$+ \frac{\left(h(x-z_0, y-w_0) \frac{(d(x,y) - i(x,y))}{n^2} \right)}{2\sigma^2}$$

$$- \left(\frac{2o(z_0, w_0)h(x-z_0, y-w_0)^2}{2\sigma^2} \right)$$

$$\sum_{x,y} \frac{2o(z_0, w_0)h(x-z_0, y-w_0)^2}{2\sigma^2} = \sum_{x,y} \frac{2o_{old}(z_0, w_0)h(x-z_0, y-w_0)^2}{2\sigma^2} +$$

$$\frac{\left(h(x-z_0, y-w_0) \frac{(d(x,y) - i(x,y))}{n^2} \right)}{2\sigma^2}$$

$$\tag{57}$$

Step 6: This results in the following update equation:

$$o_{new}(z, w) = o_{old}(z, w) + \frac{\sum_{x=1}^{N} \sum_{y=1}^{N} h(x - z, y - w)(d(x, y) - i_{old}(x, y))}{2n^2 \sum_{x=1}^{N} \sum_{y=1}^{N} h(x - z, y - w)^2} \qquad (58)$$

3.3   *Using Coarse and Fine Convergence*

Using coarse convergence followed by fine convergence is a method for quickly and accurately identifying the seeing parameter and estimate of the actual image. During the coarse convergence step, the selected EM algorithm performs iterative image estimations while searching through integer values or multiples of R_0, if the user chooses, until the algorithm converges. For example, one could do a coarse search for R_0 by multiples of two to find an estimate quicker. Next, the fine convergence begins by starting its search just before the coarse estimation value of R_0. This time, however, the algorithm performs iterations using decimal values of R_0 to narrow in on the best estimate.

This two step approach serves two distinct purposes. The first is to quickly narrow down the search area for R_0. The second purpose is to refine the search for a more accurate result for an estimated value of R_0, since not all R_0 values will be integers. Figure 14 demonstrates the process of first searching through integer values of R_0 before refining the search area.
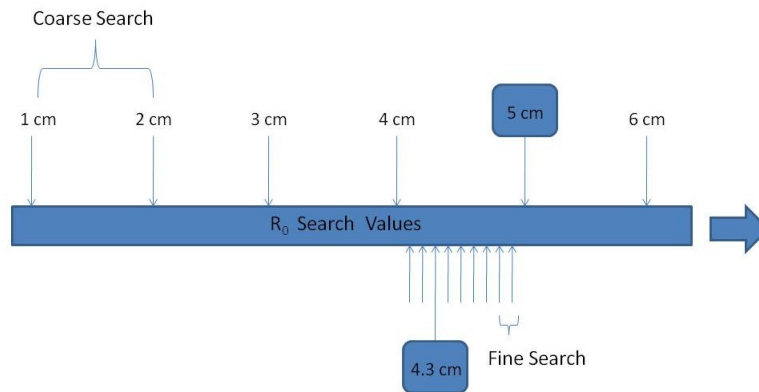

Figure 14: Diagram of the coarse and fine search method

Figures 15 through 17 demonstrate this process using simulated starfield data.

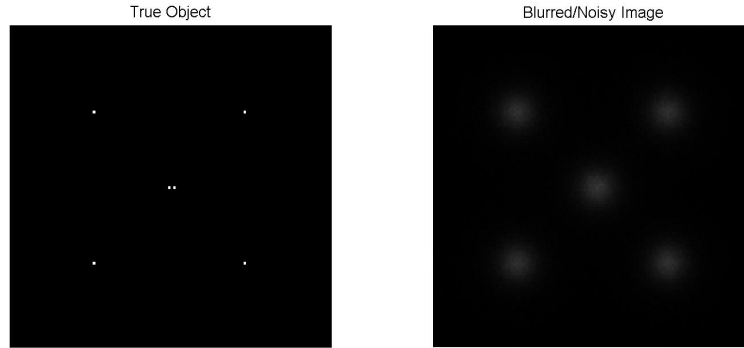
True Object   Blurred/Noisy Image

Figure 15: Short exposure blur caused by atmospheric distortion with seeing parameter of 4.3 cm and Poisson noise distribution.

Figures 16 and 17 each contain two images. The plot on the left is a snapshot of the convergence process and the image on the right reflects the updated estimate of the image based on the level of convergence. The variance of the estimated image converges with the variance of the measured image with each iteration and the image on the right is updated. There is also some key data provided with the convergence plots. The current R_0 search value, displayed above the plot, the mean squared error and the estimated number of iterations needed to converge are also updated upon each iteration. If the iterations needed exceeds the user defined level, the R_0 search value is increased and the process begins again. Once the iterations needed reaches less than 1 the process is complete and the COV method displays both the coarse and fine image results.
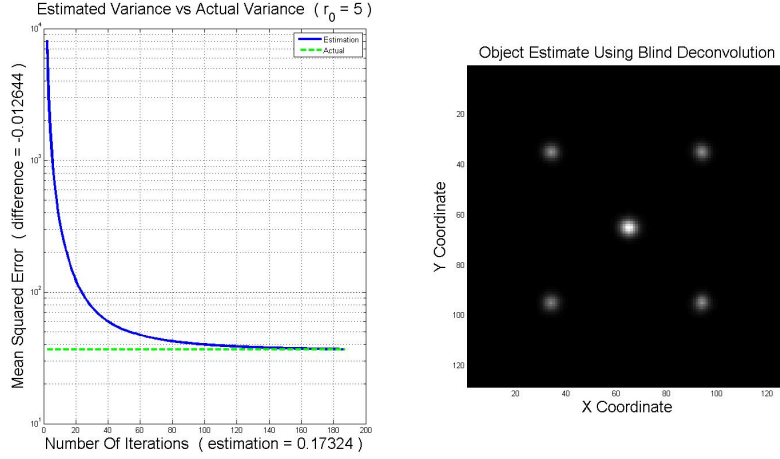
Figure 16: Coarse search by R_0 increments of 1 passed up the correct value of $R_0 = 4.3$ cm and instead stops at the best coarse value of 5 cm.
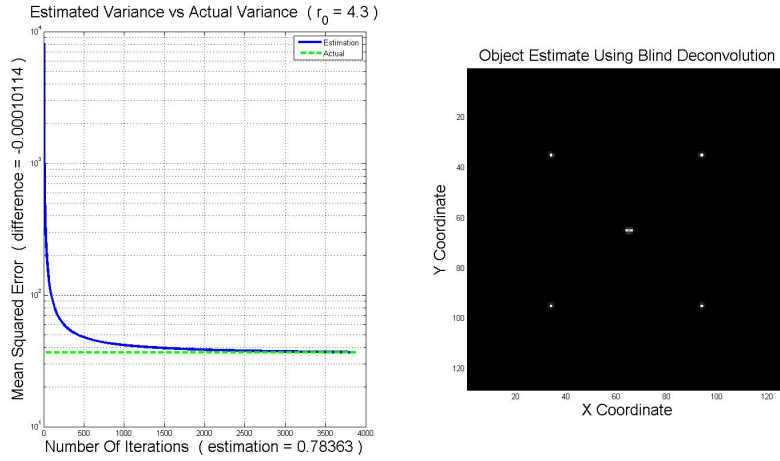

Figure 17: Fine search by R_0 increments of .1 allows for the correct value of $R_0 = 4.3$ cm to be found.

Here are some more results of the coarse and fine search method. The image below in Figure 18 depicts the true scene along with the image containing atmospheric distortion, as viewed by an optical system. Note that the two stars in the middle appear as one in the blurred image.

True Object Distorted Image

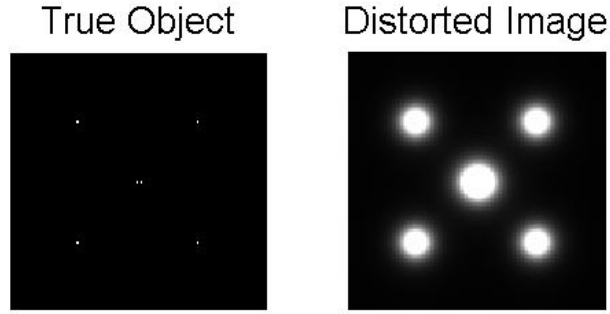Figure 18: Short exposure blur caused by atmospheric distortion with seeing parameter of 5 cm.

Figures 19, 20, and 21 below show the results of the coarse and fine convergence estimates on three sets of Gaussian distributed images with differing seeing parameters.

Coarse Search Fine Search
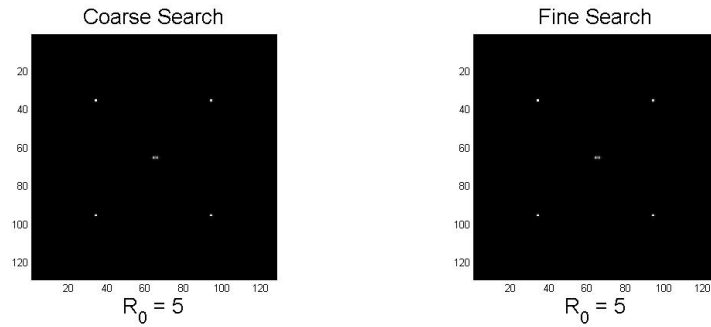
$R_0 = 5$ $R_0 = 5$

Figure 19: Side-by-side comparison using simulated star field data. Actual R_0 value is 5 cm.
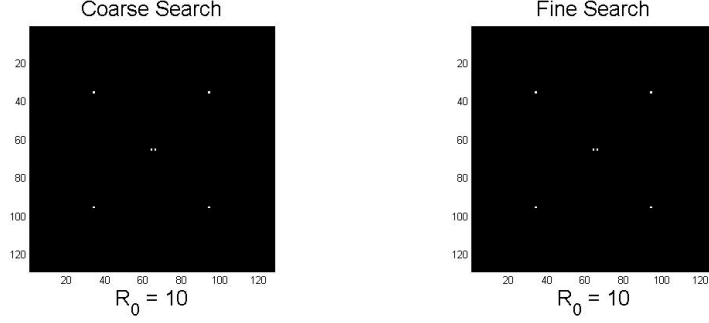
Figure 20: Side-by-side comparison using simulated star field data. Actual R_0 value is 10 cm.
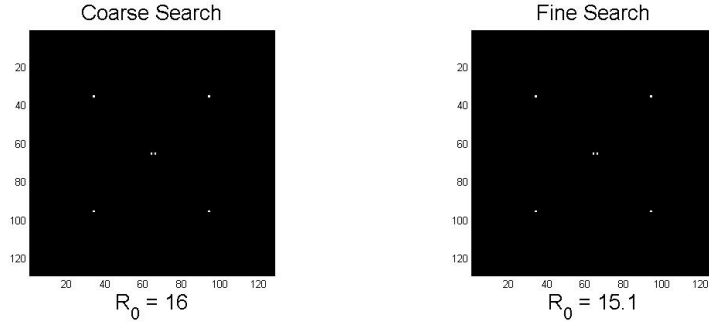
Figure 21: Side-by-side comparison using simulated star field data. Actual R_0 value is 15 cm.

In the first two figures, the coarse search was right on but in the third it overshot the correct value of R_0. The fine search was able to estimate the correct value to within 0.1 cm. These variations are all due to the the SNR ratios of the images. Both the coarse and fine search estimates are more accurate as the SNR improves.

3.4   Image Parameters Of Interest

Some key parameters which may effect the results of the COV method include the SNR and sparsity of the data, the atmospheric seeing parameter value at the time the image was acquired and the exposure type. These parameters will be explored more deeply along with sample data to support the ideas in Chapter 4. The SNR of the data may affect the ability of the COV method to accurately estimate R_0.

Different values of R_0 may also bias the results. Sparse and full scene data refer to the amount of illuminated pixels in the scene. If the COV method can produce valid results for sparse data as well as full scene data, then it will have shown improvement over the MAP estimation and APEX techniques explored in Chapter 2. Finally the exposure time of the images will be examined to see if it also has any bearing on the ability of the COV method to converge and determine the best estimate of R_0.

IV. Results and Analysis

Chapter 4 examines the effects of SNR, sparsity of the scenes, varying seeing parameter values, and exposure type and provides example simulated data. It also summarizes the results of the COV method as compared to the previous work researched in the MAP estimator and APEX algorithm. Next the results are provided for the COV method used on laboratory measured data and the idea of using the COV method on other data types is advocated. Finally, limiting factors in the effectiveness of the COV method are explored.

4.1 SNR Effects

SNR plays a key role on the convergence of the COV method. If the SNR is too low, the COV method tends to converge relatively quickly at an R_0 value which is less than the known seeing parameter of the simulated atmosphere. This quick convergence with few iterations at that R_0 value leads to heavily blurred results. As long as the SNR is high enough, the COV method does not have an issue with convergence. Figure 22 contains an image of a courtyard along the same image as it would appear if blurred by the short exposure OTF and with added Poisson noise. The same effect can be demonstrated with the starfield datasets, but the lack of illuminated pixels in the scene make it more difficult to detect the differences by eye.

True Image   Blurred Image   Noisy Image
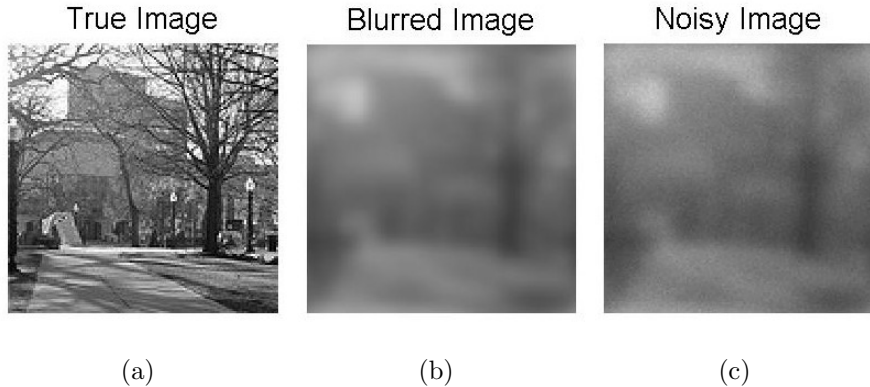
(a)   (b)   (c)

Figure 22: (a) shows the image of the true scene, (b) contains the same scene blurred with the short exposure OTF, and (c) shows the blurred image with Poisson noise.

Figure 23 shows the difference in performance of the COV method when the SNR of the observed image is varied. The SNR is scene dependent and the minimum SNR value needed to converge properly was not explored for the purposes of this research. The R_0 values in Figure 23 are the estimated values. The true value for R_0 is 5 cm.

(a) SNR = 5.7 dB
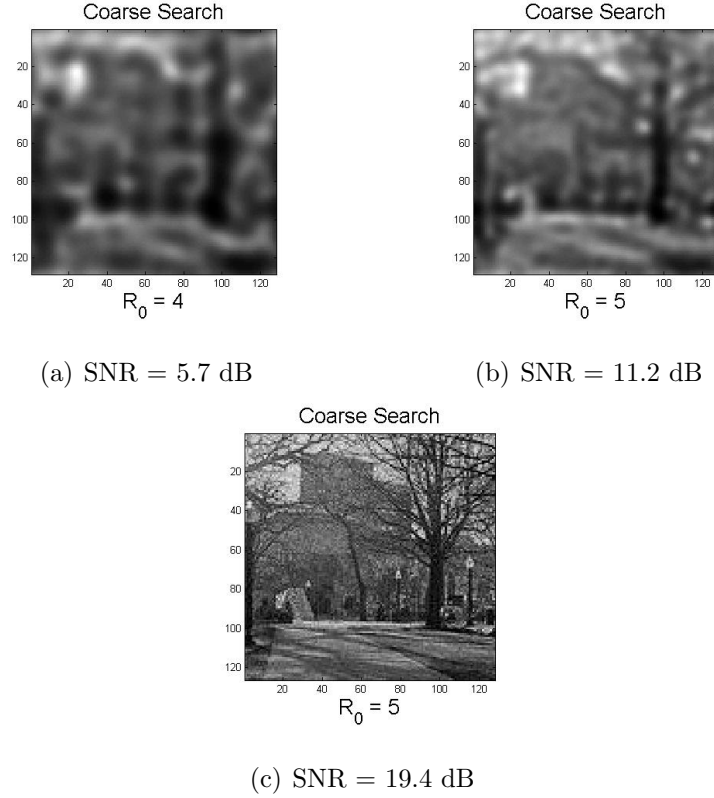

(b) SNR = 11.2 dB

(c) SNR = 19.4 dB

Figure 23: (a) The COV method estimated a lower R_0 value and converged early without enough iterations to deblur the image because the SNR was only 5.7 dB, (b) the COV method finds correct R_0 value but converges after few iterations because of low SNR of 11.2 dB, (c) SNR was increased to 19.4 dB which resulted in an image estimate that closely resembles the true image

4.2 Effect Of Different Seeing Parameters

Varying the seeing parameter values of the simulated atmosphere seemed to have no real effect on the results of the image reconstruction. The only thing that changed was the COV method took a longer amount of time to converge. The images

below in Figure 24 show the true scene and the effects of atmospheric turbulence. The next set of images in Figure 25 show the results of the same simulated star fields when using three different R_0 values.
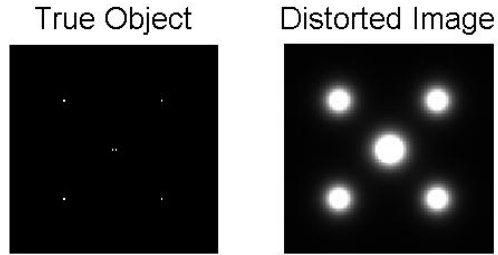

Figure 24: Here is the image of the true scene with no blurring and the same scene after being convolved with the short exposure OTF with $R_0 = 10$ cm.

(a) Actual $R_0 = 5$cm
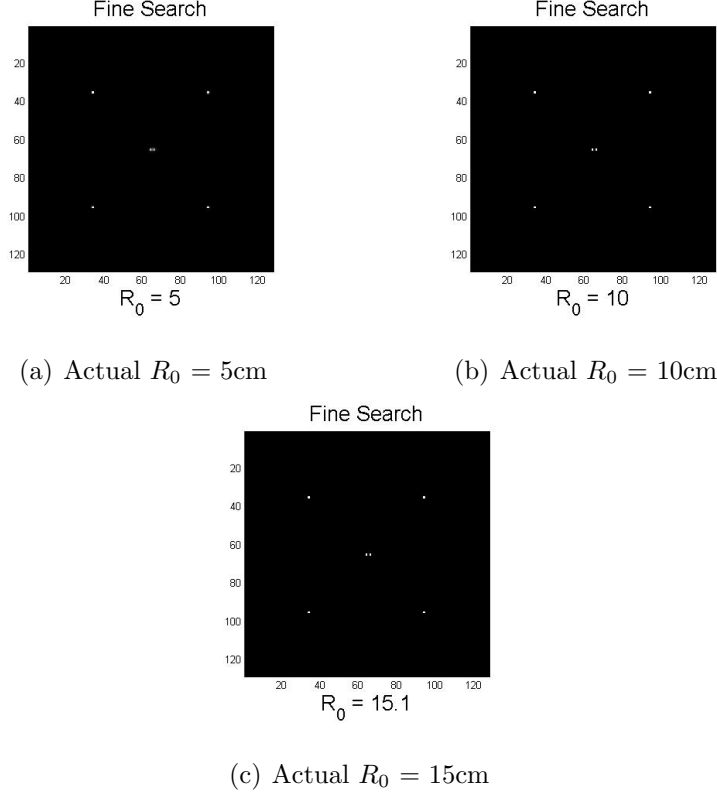(b) Actual $R_0 = 10$cm

(c) Actual $R_0 = 15$cm

Figure 25: These three images have a Gaussian distribution and were blurred with a short exposure OTF. The SNR was held constant at 18.6 dB for all three images. The images show the estimated R_0 values after being deblurred, while the labels show the actual R_0 values.

4.3   Short Vs Long Exposure

Exposure refers to the amount of light gathered or the integration period of the image. Short exposure images are typically formed by taking snapshots of a target with less than a second of integration time for the light gathering of the optical system. Long exposure images, on the other hand, are usually formed by collecting light for many seconds.

Short exposure images of astronomical scenes are far clearer as the change in the seeing parameter is negligible in such a short time. They also do not contain any blurring effects caused by the motion of the earth and the target in question.

The image below in Figure 26 depicts the true scene along with the image, containing atmospheric distortion, as viewed by an optical system. Note that the two stars in the middle appear as one in the blurred image.
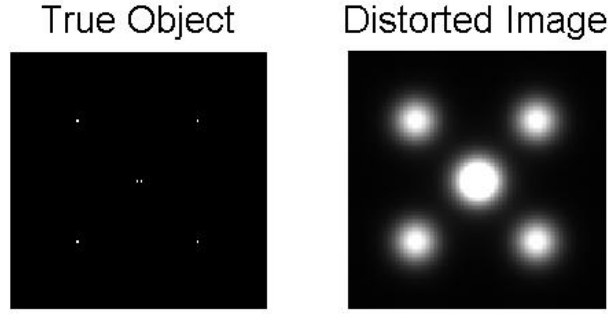

Figure 26: Long exposure blur caused by atmospheric distortion with seeing parameter of $R_0 = 5$ cm.

The simulated data below in Figures 27 and 28 contains both short and long exposure image estimates of the same star field data set. The COV method attempts to deconvolve both sets of images and estimate the true scene. The image has a Gaussian distribution and the actual R_0 value is 5 cm.
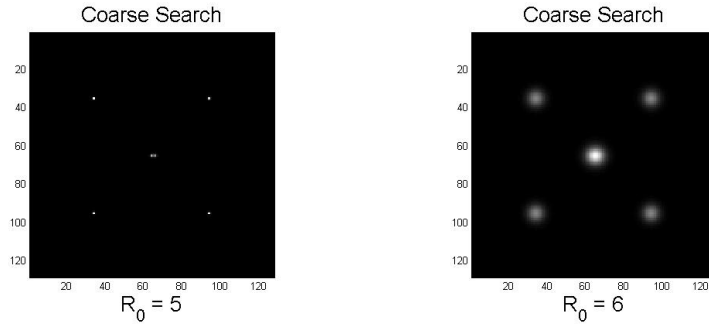

Figure 27: Short exposure(L), long exposure(R). Side-by-side comparison of the deblurred results using simulated star field data.
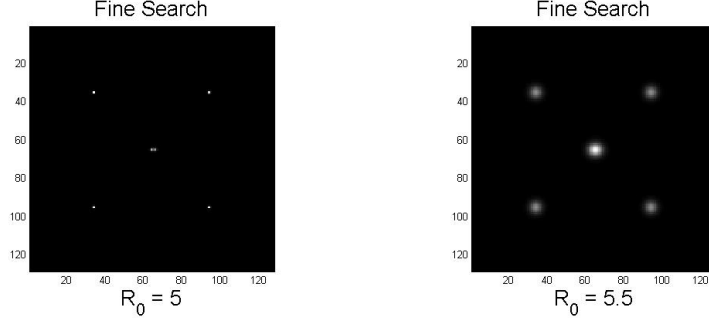
Figure 28: Short exposure(L), long exposure(R). Side-by-side comparison of the de-blurred results using simulated star field data.

The COV method was capable to accurately estimate the short exposure image with the binary pair clearly visible. The long exposure image, containing motion had too much blur and the COV method was unable to distinguish between the two stars in this case. However, it is brighter than the surrounding stars of the same intensity, indicative of its larger size.

4.4   Sparse Vs Full Scene Data

Sparse and full scene data refer to the amount of illuminated pixels in the scene. For the purpose of this research, an image with over half of its pixels illuminated is referred to as full scene and any image containing less is referred to as sparse data. Though there are many images that range in sparsity, this research focused on the extremes. The data includes binary and small star clusters as well as photographic images of a courtyard.

Chapter 2 showed how the MAP estimator was effective on full scene data but and both the MAP estimator and APEX algorithms were not accurate when processing sparse datasets. On the other hand, the COV method in this research has demonstrated effectiveness with both full scene data as seen in section 4.1 and sparse data in sections 4.2 through 4.3.

47

4.5   *Results of Laboratory Data*

Sections 1 through 3 confirmed the ability of the COV algorithm where Chapter 2 showed how the MAP estimator and APEX algorithm failed. It featured simulated data to produce results which demonstrated the desired effects for each section. Now a set of measured data obtained under laboratory conditions is provided to give support that the COV method will work on real measured data.

The data in Figure 29 is intended to represent a large celestial object such as the moon. It was captured by mounting an LED behind a bar chart in a dark room. The focusing lens was adjusted to mimic the effects of the atmosphere of the local area in Dayton Ohio, which is typically between 4 and 6 cm on a clear night.
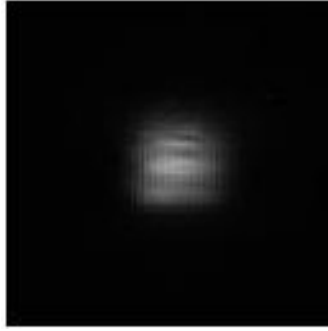
Figure 29: Target object as observed by optical system

Since this data is measured there is no way to adjust the SNR, sparsity of the scene or the OTF. The only parameter that can be manipulated is the amount of iterations that the image analyst will permit the algorithm to perform. Figures 30 through 32 show the effect that the number of iterations has on the ability of the algorithm to find the best estimate of R_0 and to deblur the image.

Coarse Search — $R_0 = 9$

Fine Search — $R_0 = 8.6$

Figure 30: The algorithm converged late because the maximum iteration allowed was too low. This image pair demonstrates the result if the user sets the max iteration level to 200.

Coarse Search — $R_0 = 7$

Fine Search — $R_0 = 6.3$

(a)

(b)
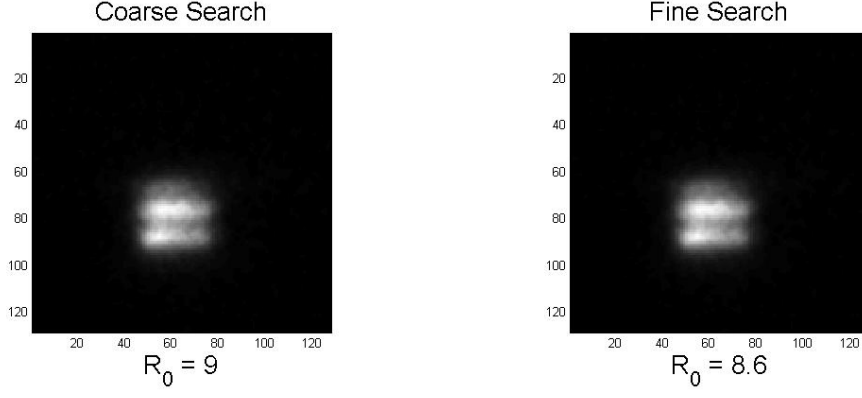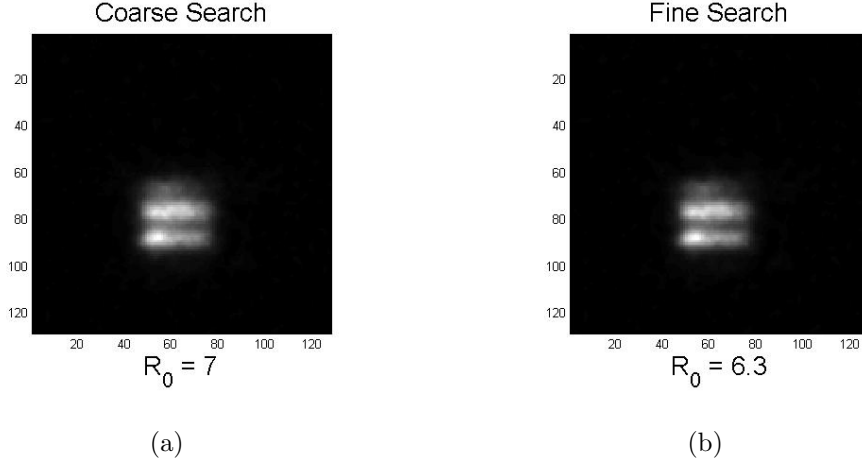
Figure 31: The algorithm still converged late because the maximum iteration allowed was too low. These images are the result of the max iteration level set to 700 but they already show improvement over figure 30.
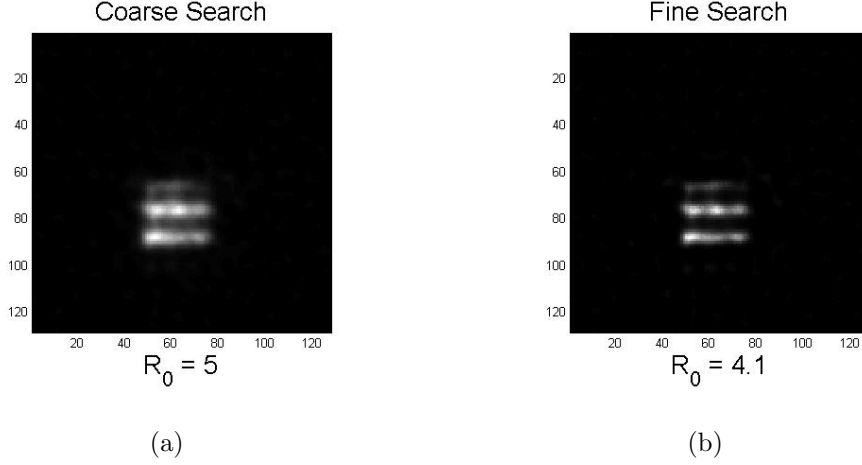
Figure 32: The algorithm was given enough iterations to converge at the best estimate of R_0 and therefore the best estimate of the target object. The max iteration level was set to 1500 but it converged way before reaching this maximum number. Therefore the algorithm would also converge at the same point for this dataset at any iteration level above 1500.

4.6 COV Method's Utility For Other Data Types

This research focused only on simulated and laboratory acquired electro-optical imagery, but this algorithm should in theory work on other types of data. As long as the blurring function and noise can be modeled it should not matter if the data is in photons or represented in the form of spectral or radar frequency returns to name a couple. As long as the correct EM equations are used, based on the distribution of the variance in the image, the COV method should be able to estimate the the target object.

4.7 Limiting Factors That Effect Results

SNR and integration time and their effects are analyzed in this section.

4.7.1 Data SNR. The SNR of an observed image is not something that can be directly controlled by the image analyst. It is determined by the the type of target, the energy source used to measure it, and the system which captures the image. The

SNR of the observed image drastically affected the results of the COV. When the SNR was too low this method was not always able to determine the correct estimate of R_0 and it tended to converge before the COV method was able to go through enough iterations to remove the blurred effects of the image.

4.7.2   Integration Time Limits.   The integration time or number of iterations, on the other hand, is up to the image analyst. The COV method while extremely accurate with a good SNR is a time consuming process. The number of iterations is controlled by the user. As long as time is not an issue, allowing the algorithm to perform more iterations will result in more accurate image estimations. Choosing a smaller number of iterations could cause the algorithm to choose a larger R_0 value than it should have, resulting in very badly blurred imagery. Sparse scenes can be processed in a matter of a few minutes but full scene data can take over a hour. This algorithm in its current form is not appropriate for any type of real-time analysis. It is better suited for post analysis of imagery.

V. Conclusions and Future Work

This section details some conclusions drawn from the results of this research. Future potential research areas are also considered below.

5.1 Conclusions

First, has been shown that the COV method works on simulated data. It was able to effectively converge for the correct atmospheric seeing parameters and recover estimates of the true images, which appeared similar to the actual images. It was able to perform effectively on fully illuminated data like both the MAP and APEX algorithms. More importantly, the COV method has been shown to work on astronomical data where the other two methods failed.

Second, it was demonstrated that this method also worked on laboratory data. This measured data was generated in a controlled laboratory environment. The focusing device of the imaging system was adjusted to produce a facsimile of our atmosphere.

Finally, the effects of parameters such as SNR, scene types, varying seeing parameters, and exposure time were investigated. These parameters were explored in a very cursory fashion. There is much work to be done in this area.

5.2 Future Work

There is much exploration left in the parameters above. For example, the effect that SNR has on image reconstruction was studied but not whether there exists a certain threshold below which this method will not perform as expected. Another area to look at may be how the COV method performs on images that may lie somewhere between sparse and full-scene. One area which was not researched was the effect of OTFs with shapes that did not fit the model.

It is also important to point out that this technique was demonstrated successfully on electro-optical data, but by no means is it limited to this narrow band of data.

It may be possible to prove that the COV method will also converge on radar data, microwaves, x-rays, etc. with the correct stopping criteria and EM update equations.

Bibliography

1. A. C. Likas, N. P. Galatsanos. "A Variational Approach for Bayesian Blind Image Deconvolution". *IEEE Transactions on Signal Processing*, Vol. 52, No. 8:2222–2233, 2004.

2. A. MacDonald, S. C. Cain and E. E. Armstrong. "Comparison Of Registration Techniques For Speckle Suppression In 2-d Lidar Image Sequences". *SPIE Conference on Image Reconstruction from Incomplete Data III 5558 . 202213.* November 2004.

3. A. P. Dempster, N. M. Laird and D. B. Rubin. "Maximum Likelihood from Incomplete Data via the EM Algorithm". *Journal of the Royal Statistical Society*, Vol. 39, No. 1:1–38, 1977.

4. Adam MacDonald Lt Col, USAF. *Blind Deconvolution Of Anisoplanatic Images Collected By A Partially Coherent Imaging System.* Ph.D. thesis, Air Force Institute Of Technology, 2006.

5. Alfred S. Carasso, David S. Bright and Andras E. Vladar. "APEX Method And Real-time Blind Deconvolution Of Scanning Electron Microscope Imagery". *Optical Engineering*, Vol. 41, No. 10, October 2002.

6. Ce Liu, Richard Szeliski, William T. Freeman and Sing Bing Kang. "Noise Estimation From A Single Image". 2006.

7. D. A. Fish, A. M. Brinicombe and E.R. Pike. "Blind Deconvolution By Means Of The Richardson-lucy Algorithm". *Journal of the Optical Society of America*, Vol. 12:5865, January 1995.

8. Goodman, Joseph W. *Statistical Optics.* John Wiley & Sons, INC., 2000.

9. Leon-Garcia, Alberto. *Probability, Statistics, and Random Processes for Electrical Engineering.* Pearson Education, INC., 2008.

10. Loyev, Vadim and Yitzhak Yitzhaky. "Initialization Of Iterative Parametric Algorithms For Blind Deconvolution Of Motion-blurred Images". *Applied Optics*, Vol. 45, No. 11:2444–2452, 2006.

11. R. Salakhutdinov, S. T. Roweis and Z. Ghahramani. "Optimization with EM and Expectation-Conjugate Gradient". *International Conference on Machine Learning*, Vol. 20:672–679, 2003.

12. X. Huang, A. C. Madoc and A. D. Cheetham. "Image Multi-Noise Removal By Wavelet-Based Bayesian Estimator". *Circuits and Systems*, Vol. 3:2699 – 2702, 2005.

REPORT DOCUMENTATION PAGE

1. REPORT DATE *(DD–MM–YYYY)*	2. REPORT TYPE		3. DATES COVERED *(From — To)*
24–03–2011	Master's Thesis		Sept 2009 — Mar 2011

4. TITLE AND SUBTITLE

Blind Deconvolution Method Of
Image Deblurring Using
Convergence Of Variance

5a. CONTRACT NUMBER

5b. GRANT NUMBER

5c. PROGRAM ELEMENT NUMBER

6. AUTHOR(S)

Quentin MacManus, Captain, USAF

5d. PROJECT NUMBER

None

5e. TASK NUMBER

5f. WORK UNIT NUMBER

7. PERFORMING ORGANIZATION NAME(S) AND ADDRESS(ES)

Air Force Institute of Technology
Graduate School of Engineering and Management (AFIT/EN)
2950 Hobson Way
WPAFB OH 45433-7765

8. PERFORMING ORGANIZATION REPORT NUMBER

AFIT/GE/ENG/11-26

9. SPONSORING / MONITORING AGENCY NAME(S) AND ADDRESS(ES)

Maj David M. Strong
Air Force Research Lab, AFRL/RDSMA
535 Lipoa Pkwy.
Kihei, Hawaii 96753
Phone: 808-891-7753
david.strong@maui.afmc.af.mil

10. SPONSOR/MONITOR'S ACRONYM(S)

11. SPONSOR/MONITOR'S REPORT NUMBER(S)

12. DISTRIBUTION / AVAILABILITY STATEMENT

APPROVED FOR PUBLIC RELEASE; DISTRIBUTION UNLIMITED.

13. SUPPLEMENTARY NOTES

This material is declared a work of the U.S. Government and is not subject to copyright protection in the United States.

14. ABSTRACT

Images are used for both aerial and space imagery applications, including target detection and tracking. The current problem concerning objects in geosynchronous orbit is that they are dim and hard to resolve because of their distance. This work will further the combined effort of AFIT and AFRL to provide enhanced space situational awareness (SSA) and space surveillance. SSA is critical in a time when many countries possess the technology to put satellites into orbit. Enhanced imaging technology improves the Air Force's ability to see if foreign satellites or other space hardware are operating in the vicinity of our own assets at geosynchronous orbit. Image deblurring or denoising is a crucial part of restoring images that have been distorted either by movement during the capture process, using out-of-focus optics, or atmospheric turbulence. The goal of this work is to develop a new blind deconvolution method for imaging objects at geosynchronous orbit. It will feature an expectation maximization (EM) approach to iteratively deblur an image while using the convergence of the image's variance as the stopping criteria.

15. SUBJECT TERMS

16. SECURITY CLASSIFICATION OF:			17. LIMITATION OF ABSTRACT	18. NUMBER OF PAGES	19a. NAME OF RESPONSIBLE PERSON
a. REPORT	b. ABSTRACT	c. THIS PAGE			Richard K. Martin, (ENG)
U	U	U	UU	67	**19b. TELEPHONE NUMBER** *(include area code)* (937) 255–3636, x4625; Richard.martin afit.edu